Fatigue fracture mechanics in gold-based MEMS notched specimens: experimental and numerical study

Journal of Micromechanics and Microengineering

PAPER • **OPEN ACCESS**

Fatigue fracture mechanics in gold-based MEMS notched specimens: experimental and numerical study

To cite this article: Francesca Pistorio and Aurelio Somà 2023 *J. Micromech. Microeng.* **33** 085012

OPEN ACCESS
IOP Publishing
Journal of Micromechanics and Microengineering
J. Micromech. Microeng. **33** (2023) 085012 (21pp)
https://doi.org/10.1088/1361-6439/acddf3

Fatigue fracture mechanics in gold-based MEMS notched specimens: experimental and numerical study

Francesca Pistorio* **and Aurelio Somà**

Department of Mechanical and Aerospace Engineering, Politecnico di Torino, Corso Duca degli Abruzzi 24, 10129 Turin, Italy

E-mail: francesca.pistorio@polito.it

Received 28 February 2023, revised 19 May 2023
Accepted for publication 13 June 2023
Published 6 July 2023

Abstract

The characterization of fatigue fracture mechanics in gold-MEMS notched specimens is presented in this work. A test microstructure with a central notched specimen is specifically designed and built to perform on-chip fatigue test. The central specimen undergoes cyclic loading due to the application of alternating voltage. The variation in the microstructure deflection is measured using an optical profilometer and is attributed to the crack growth in the gold material, causing the variation in the specimen stiffness. The occurrence of pull-in condition is used as a fracture detector, then the fracture of the specimen can be recognized without performing scanning electron microscope inspections during the fatigue test. Crack propagation in the test specimen is simulated through a coupled-field electromechanical fracture finite element model and the resulting crack path is compared to the experimental measurments performed with scanning electron microscope analyses. Finally, Paris' law is applied and the number of cycles to failure is computed by exploiting the results of the fracture model and experimental measurements. Both experimental and numerical results demonstrate that the notch acts as a stress and strain raiser, fostering crack nucleation, and that the linear elastic fracture mechanics theory is still valid to describe crack propagation in micro-size samples.

Keywords: microelectromechanical systems (MEMS), linear elastic fracture mechanics (LEFM), Paris' law, fatigue, notch, multiphysics simulation, finite element method (FEM)

(Some figures may appear in colour only in the online journal)

1. Introduction

In recent years, micro-electro-mechanical systems (MEMS) devices have become a well-established technology, given the growing need for integrated and miniaturized systems with advanced functionality [1, 2].

The advantages of MEMS devices lie in their low cost, small size, lightweight, low power consumption, high reliability, easy integration, and suitability for harsh working environments [3–6]. Then, MEMS devices are employed in a wide range of applications and fields, from industrial to consumer areas [7–10], being also recently attractive in the field of the Internet Of Things technology [11, 12].

The problem of reliability and durability is a central theme in the field of MEMS research, especially in those applications where high-reliability performance under harsh field

* Author to whom any correspondence should be addressed.

Table 1. Summary of the main works existing in the literature dealing with fatigue in MEMS devices.

Material	Loading strategy	Goals	References
Gold	Electrostatic actuation	Fatigue characterization of microbeam through pull-in monitoring	[28–32]
Gold	Electrostatic actuation	Effect of mean stress on fatigue of microbeam	[33]
Polysilicon	Electrostatic actuation	Fatigue lifetime prediction using Paris' law	[39]
Polysilicon	Electrostatic actuation	Characterization of fatigue in microbeam	[34]
Polysilicon	Electrostatic actuation	Fatigue test on micro-cantilever beams	[35]
Silicon	Electrostatic actuation	Fatigue and fracture characterization of microbeam	[40]
Silicon	Electrostatic actuation	Fatigue characterization of bending and torsion in microstructures	[36]
Tungsten and metallic glass	In-situ indenter	Measurement of the cyclic crack growth rate in notched specimen and Paris' law application	[20]
LIGA Nickel	Piezoelectric actuation	Fatigue characterization and lifetime prediction of notched specimen using Paris' law	[38]
Ni–P amorphous alloy	Mechanical testing machine for micro-sized specimens	Fatigue fracture test on notched specimen	[37]

conditions is required, such as medical, automotive, and aerospace applications.

The reliability assessment in MEMS devices is a challenging task since MEMS devices are miniaturized systems integrating both electronic and mechanical components, then the device failure may be caused both by mechanical and electric reasons [13].

Fatigue is one of the major cause of failure in MEMS devices [14]. Generally speaking, fatigue is caused by repeated cyclic loads, leading to crack initiation and propagation from initial micro-defects in the material, resulting in the complete fracture of the component ultimately.

Fatigue in MEMS devices could arise due to the fluctuation in applied stress or strain [15], as well as due to temperature variation [16, 17], and chemically aggressive or embrittling environment [18] which can create or accelerate crack growth.

It is well known that the fatigue behaviour of a structure strictly depends on the material characteristics. Furthermore, the mechanical properties of microstructural materials can be affected by the fabrication process and may differ from those of bulk materials [19, 20]. Therefore, there is the need to properly characterize the fatigue behaviour of micro-components in order to design reliable MEMS devices.

The characterization of the fatigue fracture behaviour of samples at the micro-scale is challenging, both from an experimental and modelling point of view.

Fracture toughness and fatigue properties in macro-sized specimens are measured according to ASTM standards, however, there are no standards for micro-sized specimens.

Furthermore, the approaches commonly used in traditional macro-scale mechanics cannot be adopted to perform fatigue testing at the micro-scale because of two main reasons. Firstly, it is not easy to decouple the characterization of the specimen material from the machine soliciting it. Secondly, the development of test microstructures is challenging because proper alignment, as well as gripping, loading of the specimen, and minimization of residual stresses due to the fabrication process have to be addressed during the test. For this reasons, the so-called on-chip fatigue testing is often used instead of off-chip testing. Then, specific test microstructures are designed to load and measure the resulting deformation of the test specimen on the same chip, without employing external instrumentation.

Finally, some authors [21–24] have evidenced the breakdown of the traditional fracture mechanics theory at a very small scale.

The fatigue behaviour of the material is generally described using two different approaches: the *S*–*N* (or Wöhler) curve, which correlates the applied mechanical stress (or strain) to the fatigue life, and Paris' law, which describes the growth of cracks in the material based on the linear elastic fracture mechanics (LEFM) theory [25–27].

Different attempts to obtain Wöhler curves of micromechanical samples were made [28–36], on the other hand, few works applying Paris' law to characterize fatigue fracture process in MEMS devices exist in the literature [20, 37–39].

Table 1 summarizes the main works existing in the literature dealing with fatigue in MEMS devices. Different materials were analyzed, as well as several test microstructures were proposed, and different strategies to load the test specimen were adopted, according to on-chip and off-chip testing.

Modelling the fatigue fracture in MEMS devices requires solving a multiphysics problem, which is often high-demanding from the computational point of view, especially in a three-dimensional (3D) model.

Different numerical methods have been proposed in the literature to solve multiphysics fracture problems, such as phase-field model (PFM) [41], cohesive elements model (CZM) [42], and extended finite element method (XFEM) [43]. Alternatively, crack propagation is simulated by computing stress intensity factors (SIFs) through the J-integral or energy release rate using finite element method (FEM), on the basis of LEFM theory [44].

This paper aims to characterize the fatigue fracture behaviour of gold-based MEMS notched specimens, both from

experimental and modelling point of view. A test microstructure with a notched central specimen is specifically designed to perform on-chip fatigue test. The kinematic model, as well as the experimental setup and the multiphysics FEM fracture model, are presented. The test notched specimen is cyclically loaded at different stress levels using electrostatic actuation. The variation in the microstructure deflection is monitored during the test and correlated to the stiffness variation caused by crack propagation in the material. The occurrence of the pull-in phenomenon is used as a failure detector, then the specimen is not inspected during the test. The crack propagation path is observed using scanning electron microscope (SEM) after the specimen failure. A comparison between the crack path obtained from the fracture model and measured experimentally is performed. Finally, the fatigue life cycle is computed by applying Paris' law and compared to the experimental results.

2. Material and methods

2.1. Test microstructure design

A test microstructure is specifically designed and built to characterize the fatigue fracture in gold-based MEMS notched specimen with on-chip testing. The design of the test microstructure, as well as its fabrication process and the advantages over other designs proposed in the literature, are extensively reported in authors' previous works [32, 33, 45–47], thus just a brief description is given below for the sake of clarity.

The schematic and the SEM image of the test microstructure are shown in figure 1.

The effective dimensions of the test microstructure are measured with the high-resolution optical interferometric profilometer ZoomSurf3D by Fogale Nanotech and are reported in table 2.

The test microstructure is composed of two suspended perforated plates, anchored at the external edges to the substrate by eight trapezoidal flexural beams.

A test specimen with a rectangular cross-section is located at the centre of the microstructure and connected with the two suspended plates with rounded corners to avoid local stress concentration effects. The specimen has a circumferential notch in the centre, which acts as local stress and strain raisers.

The suspended plates can move and act as electrostatic actuators, and the flexural beams are structural hinges subjected to a uniform stress distribution when they are loaded by bending moment thanks to their trapezoidal shape.

Two bottom actuation electrodes are fixed on the substrate without covering the full area under the top suspended plates, which allows for maximizing displacement and stress in the central specimen before the occurrence of the pull-in phenomenon. Furthermore, the bottom electrodes are located at a distance of 25 μm from the flexural beams to avoid local plasticity in the beams.

The test specimen is a clamped-clamped microbeam subjected to tensile load when the actuation voltage is applied between the top suspended plates and bottom electrodes. In this case, the suspended plates move downwards and undergo a symmetrical rigid rotation thanks to the trapezoidal flexural beams, loading the central specimen ultimately.

The microstructure is fabricated using thin film gold material according to RF Switch Surface Micromachining (RFS) process developed by Bruno Kessler Foundation [48, 49]. The moving parts of the microstructure are built through a two-step gold electroplating process over a photoresist of 3 μm thickness, resulting in thicker and stiffer suspended plates compared to the central specimen. A summary of RFS microfabrication process steps is widely described in [28, 50, 51]. It is important to point out that the fabrication process is designed to limit the onset of residual stress, as explained in detail in previous authors' works [45, 46, 52].

2.2. Mathematical model

2.2.1. Kinematic model of the test microstructure. The design of the test microstructure is addressed to correlate the degradation of the specimen stiffness due to cycling to the variation in the device deflection, as previously reported in [32, 33, 47]. The kinematic scheme of the test microstructure is shown in figure 2.

The electrostatic force (F_e) acting on each suspended plate and caused by the application of the actuation voltage (V) between the top suspended plates and the bottom electrodes is expressed according to equation (1).

$$F_e = \frac{\varepsilon_0 A V^2}{2\left(g_0 - h_1\right)^2} \tag{1}$$

where ε_0 is the permittivity, $A = l_e w_e$ is the overlap area, l_e and w_e are the length and width of the bottom electrodes respectively, g_0 is the initial air gap thickness and h_1 is the downward deflection at the centre of the top suspended plates.

The electrostatic force causes the plates to rigidly rotate by α angle, resulting in the horizontal ($\Delta l/2$) and vertical (h_2) displacement of the specimen anchors. Then, the horizontal displacement cause the axial force (P), on the other hand, the vertical displacement causes the bending moment (M). Finally, the resulting axial stress in the central specimen is computed according to equation (2).

$$\sigma_a = \sigma_{a,P} + \sigma_{a,M} \tag{2}$$

where $\sigma_{a,P}$ is the axial stress component due to the axial force P and is computed according to equation (3*a*), and $\sigma_{a,M}$ is the axial stress component due to bending moment M and is computed according to equation (3*b*).

$$\sigma_{a,P} = \frac{P}{A_s} = \frac{2E}{l_s}\left(l_d - \sqrt{l_d^2 - h_2^2}\right) \tag{3a}$$

$$\sigma_{a,M} = \frac{M z_s}{2J} = \frac{3E z_s}{2l_s}\alpha = \frac{3E z_s}{2l_s}\sin^{-1}\frac{h_2}{w_p} \tag{3b}$$

where E is the Young modulus, A_s is the specimen cross-section, l_s is the specimen length, P is the axial force, $M = \frac{3EJ}{l_s}$

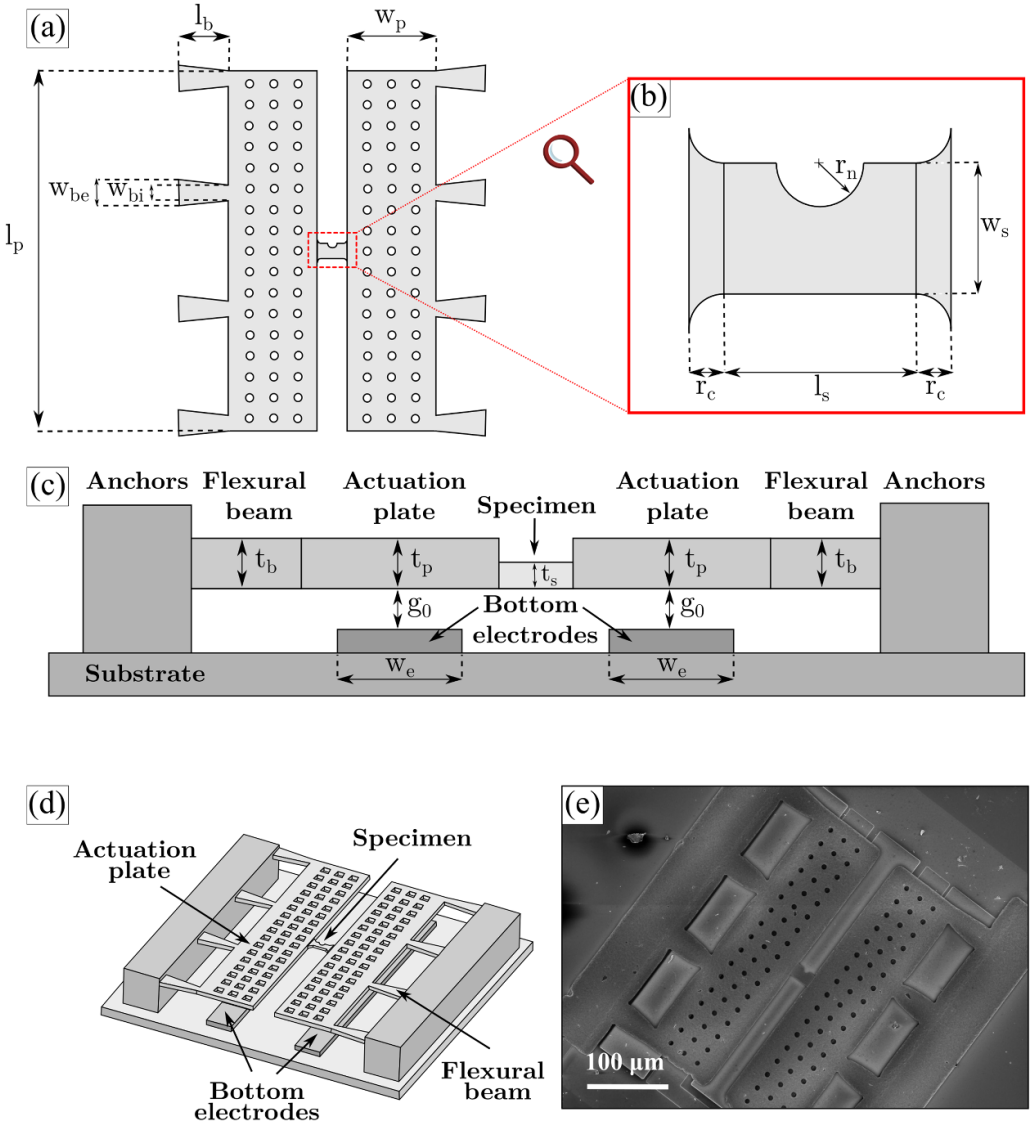

Figure 1. Design of the test microstructure with central notched specimen for fatigue fracture test. (a) Schematic top and (c) side views, with detail of (b) central specimen, showing the dimensions. (d) Schematic view and (e) SEM image of the whole test microstructure.

is the bending moment, $J = \frac{w_s t_s^3}{12}$ is the bending moment of inertia, w_s and t_s are the specimen width and thickness respectively, and z_s is the coordinate along the specimen thickness.

The maximum stress at the notch root ($\sigma_{n,max}$) is computed from the nominal axial stress (σ_a) as long as stress and strain at the notch root remain elastic, according to equation (4).

$$\sigma_{n,max} = K_t \sigma_a \tag{4}$$

where K_t is the elastic stress concentration factor.

The vertical deflection of the centre of the specimen with respect to the edge due to bending moment can be neglected as it is much lower than the overall structure vertical displacement (h_2). As a consequence, the proposed test microstructure allows correlating the microstructure vertical displacement, the nominal axial stress in the central specimen (equations (2) and (3)) and the maximum axial stress at the notch root (equation (4)).

Furthermore, the variation of the vertical displacement measured during the fatigue test is attributed to the variation in the device stiffness due to the crack growth at the notch. This is quite reasonable for three reasons: (1) the central specimen is the most stressed component of the microstructure, as also demonstrated by FEM analysis; (2) the notch acts as a stress raiser, fostering crack nucleation [42, 47]; (3) the plates and flexural beams are less affected by damage, as also confirmed by SEM analyses and by results from previous works [32, 33].

Finally, the specimen failure is identified by the instantaneous large variation of the microstructure displacement (h_2) without inspecting the specimen when loaded, as the device undergoes pull-in condition when the specimen fractures [28, 52, 53].

2.2.2. Fundamentals of linear elastic fracture mechanics (LEFM) theory. LEFM theory is used to describe the stress state near the crack tip region when the material is linear and

Table 2. Test microstructure and central specimen dimensions measured using the optical interferometric profilometer ZoomSurf3D by Fogale Nanotech.

Parameters	Value	Unit
Specimen length (l_s)	22	μm
Specimen width (w_s)	15	μm
Specimen thickness (t_s)	1.8	μm
Specimen to plate connection radius (r_c)	4	μm
Notch root radius (r_n)	5	μm
Actuation plate length (l_p)	350	μm
Actuation plate width (w_p)	85	μm
Actuation plate thickness (t_p)	5.2	μm
Hole side dimension	7.8	μm
Number of holes per actuation plate	17×3	—
Supports length (l_b)	48.2	μm
Supports internal width (w_{bi})	14.8	μm
Supports external width (w_{be})	24.8	μm
Supports thickness (t_b)	5.2	μm
Lower electrodes length (l_e)	350	μm
Lower electrodes width (w_e)	35	μm
Initial air gap thickness (g_0)	3.2	μm

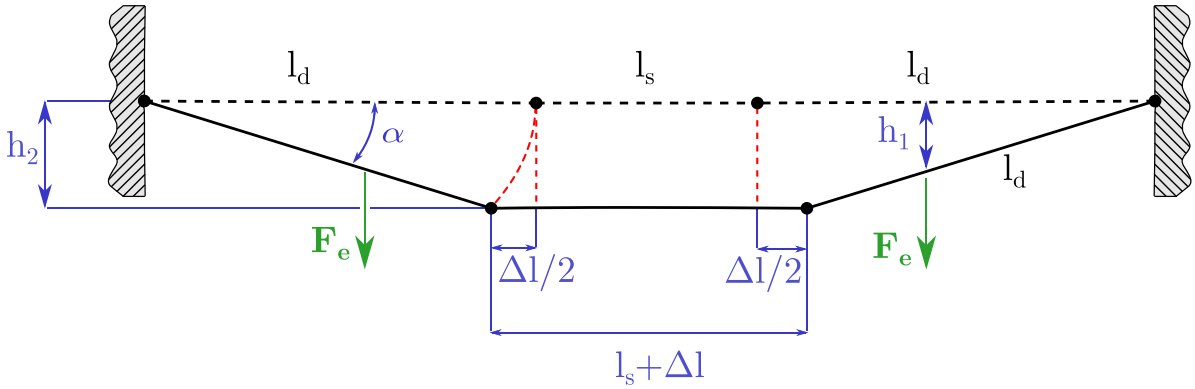

Figure 2. Kinematic scheme of the test microstructure, where l_s and Δl are the initial length and the total horizontal elongation of the central specimen respectively, h_1 and h_2 are the downwards deflection of the top suspended plate at the centre and at the edge respectively, $l_d = w_p + l_b$ and α is the rotation of the top suspended plate.

elastic or when the assumption of small-scale yielding holds, i.e. when the extension of the plastic zone at the crack tip is negligible as compared to the crack dimensions.

According to LEFM, the stress at the crack tip goes to infinite and the SIF is generally adopted to compute the stress field (σ_{ij}) at the crack tip, according to equation (5) [54].

$$\sigma_{ij} = \frac{K}{\sqrt{2\pi r}} f_{ij}(\theta) \tag{5}$$

where K is the SIF, r and θ are the polar coordinates in the frame with the origin at the crack tip (figure 3(a)) and $f_{ij}(\theta)$ is a dimensionless shape function.

In the case of arbitrary loading, the stress field is expressed as the superposition of three fracture modes (figure 3(b)), namely mode I (Opening), mode II (Sliding) and mode III (Tearing) [55], according to equation (6).

$$\sigma_r = \frac{K_I}{4\sqrt{2\pi r}}\left[5\cos\left(\frac{\theta}{2}\right) - \cos\left(\frac{3\theta}{2}\right)\right] - \frac{K_{II}}{4\sqrt{2\pi r}}\left[5\sin\left(\frac{\theta}{2}\right) - \sin\left(\frac{3\theta}{2}\right)\right] \tag{6a}$$

$$\sigma_\theta = \frac{K_I}{4\sqrt{2\pi r}}\left[3\cos\left(\frac{\theta}{2}\right) + \cos\left(\frac{3\theta}{2}\right)\right] + \frac{K_{II}}{4\sqrt{2\pi r}}\left[3\sin\left(\frac{\theta}{2}\right) + 3\sin\left(\frac{3\theta}{2}\right)\right] \tag{6b}$$

$$\tau_{r\theta} = \frac{K_I}{4\sqrt{2\pi r}}\left[\sin\left(\frac{\theta}{2}\right) + \sin\left(\frac{3\theta}{2}\right)\right] - \frac{K_{II}}{4\sqrt{2\pi r}}\left[\cos\left(\frac{\theta}{2}\right) - 3\cos\left(\frac{3\theta}{2}\right)\right] \tag{6c}$$

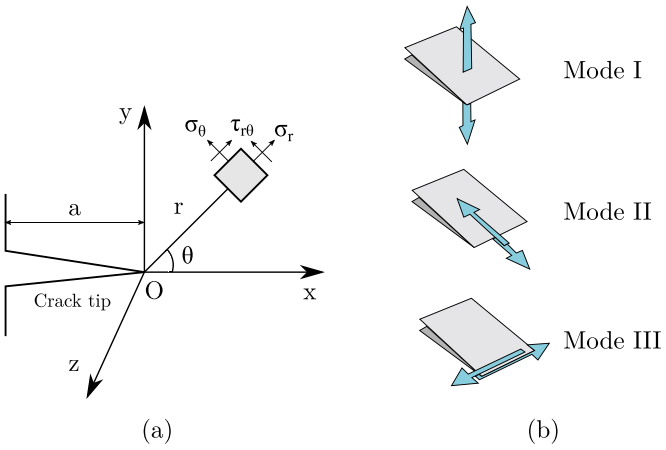

Figure 3. (a) Stress field near the crack tip in polar coordinates and (b) the three fracture modes.

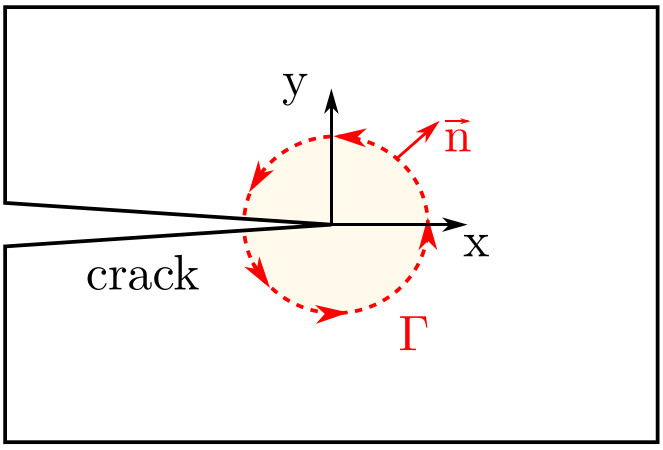

Figure 4. Schematic of the crack region, where Γ is an arbitrary counterclockwise path surrounding the crack tip, x, y are the coordinate directions and n is the versor normal to Γ.

$$\tau_{rz} = \frac{K_{\mathrm{III}}}{\sqrt{2\pi r}} \sin\left(\frac{\theta}{2}\right) \tag{6d}$$

$$\tau_{\theta z} = \frac{K_{\mathrm{III}}}{\sqrt{2\pi r}} \cos\left(\frac{\theta}{2}\right) \tag{6e}$$

$$\sigma_z = \begin{cases} \nu(\sigma_r + \sigma_\theta) = \frac{2\nu}{\sqrt{2\pi r}}\left[K_{\mathrm{I}} \cos\left(\frac{\theta}{2}\right) - K_{\mathrm{II}} \sin\left(\frac{\theta}{2}\right)\right] & \text{plane strain} \\ 0 & \text{plane stress} \end{cases} \tag{6f}$$

where K_i is the SIF of mode i and ν is the Poisson ratio.

For a given mode i, the K_i is a function of the corresponding energy release rate (G_i), which is the decrease in the total potential energy of the system per increase in fracture length (or surface area for 3D problems), according to equation (7) [56].

$$K_{\mathrm{I}} = \begin{cases} \sqrt{EG_{\mathrm{I}}} & \text{plane stress} \\ \sqrt{\dfrac{EG_{\mathrm{I}}}{(1-\nu^2)}} & \text{plane strain} \end{cases} \tag{7a}$$

$$K_{\mathrm{II}} = \sqrt{\frac{EG_{\mathrm{II}}}{(1-\nu^2)}} \tag{7b}$$

$$K_{\mathrm{III}} = \sqrt{\mu G_{\mathrm{III}}} \tag{7c}$$

where G_i is the energy release rate of mode i and μ is the shear modulus. In the case of mixed-mode, the energy release rate (G) is computed by applying the superposition principle, according to equation (8).

$$G = G_{\mathrm{I}} + G_{\mathrm{II}} + G_{\mathrm{III}} \tag{8}$$

SIF is often computed numerically from the energy release through the J-integral when LEFM theory holds, as the J-integral is equal to the energy release rate.

The J-integral for a 2D fracture problem is expressed in equation (9), considering an arbitrary counterclockwise path Γ around the crack tip (figure 4) [57].

$$J = G = \int_{\Gamma} \left(\psi_{\mathrm{el}} dy - t_i \frac{\partial u_i}{\partial x}\right) ds \tag{9}$$

where $\psi_{\mathrm{el}} = \int_0^{\varepsilon_{ij}} \sigma_{ij} d\varepsilon_{ij}$ is the elastic strain energy density, σ_{ij} are the components of the stress tensor, ε_{ij} are the components of the strain tensor, $t_i = \sigma_{ij} n_j$ are the components of the traction vector acting on the path Γ, n_j is the versor normal to Γ, u_i are the components of the displacement vector, x and y are the coordinates parallel and perpendicular to the crack direction respectively, and ds is the element length along Γ.

The contributions of different modes cannot be directly distinguished from J-integral in the case of mixed-mode fracture. In this case, the interaction energy integral method initially proposed by Yau *et al* [58] is largely used to compute mixed-mode SIFs separately, being implemented in most commercial FEM software, such as Ansys and Abaqus. Further details on the interaction integral method and its numerical implementation are reported in [59].

2.3. Fatigue crack growth

Fatigue refers to the progressive failure of materials due to crack initiation and propagation during repeated cyclic loading. Fatigue crack growth is generally divided into three stages, as shown in figure 5 [56]. First, macro-cracks nucleate from material imperfections, such as voids and micro-defects (Stage I), then stable crack propagation occurs (Stage II), followed by unstable crack propagation (Stage III), which rapidly leads to final failure.

Paris' law is the most popular power law used to describe stable crack growth (Stage II). The crack growth rate $\left(\frac{da}{dN}\right)$ is a function of the SIF range (ΔK), defined in equation (10), according to equation (11) [25–27].

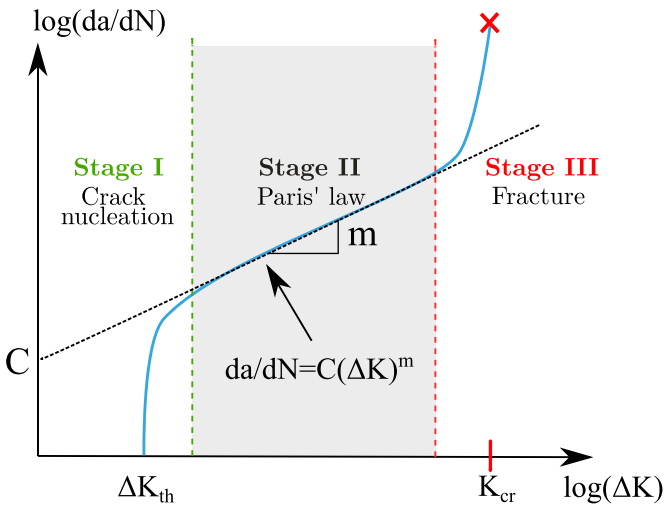

Figure 5. The three phases of fatigue crack growth: crack nucleation (Stage I), stable crack growth (Stage II) where Paris' law holds and final fracture (Stage III).

Table 3. Most common expressions of equivalent SIF range (ΔK_{eqv}) in the literature, where θ_c is the crack propagation angle, ΔK_I and ΔK_{II} are the mode I and II SIF range, respectively.

Author	ΔK_{eqv}		References
Tanaka	$\left(\Delta K_I^2 + 2\Delta K_{II}^2\right)^{\frac{1}{2}}$	(15)	[60]
Tanaka	$\left(\Delta K_I^4 + 8\Delta K_{II}^4\right)^{\frac{1}{4}}$	(16)	[60]
Irwin *et al*	$\left(\Delta K_I^2 + \Delta K_{II}^2\right)^{\frac{1}{2}}$	(17)	[61]
Yan *et al*	$\frac{1}{2}\cos\frac{\theta_c}{2}\left[\Delta K_I(1+\cos\theta_c) - 3\Delta K_{II}\sin\theta_c\right]$	(18)	[62]
Richard *et al*	$\frac{\Delta K_I}{2} + \frac{1}{2}\left[\Delta K_I^2 + 4(1.155\Delta K_{II})^2\right]^{\frac{1}{2}}$	(19)	[55]
Demir *et al*	$\left(1.0519\Delta K_I^4 - 0.035\Delta K_{II}^4 + 2.3056\Delta K_I^2\Delta K_{II}^2\right)^{\frac{1}{4}}$	(20)	[63]
Hussain *et al*	$\sqrt{\frac{4}{(3+\cos^2\theta_c)^2}\left(\frac{1-\theta_c/\pi}{1+\theta_c/\pi}\right)^{\theta/\pi}\left[(1+3\cos^2\theta_c)\Delta K_I^2 + 4\sin 2\theta_c\Delta K_I\Delta K_{II} + (9-5\cos^2\theta_c)\Delta K_{II}^2\right]}$	(21)	[64]

$$\Delta K = K_{max} - K_{min} = (1-R)K_{max} \tag{10}$$

$$\frac{da}{dN} = C\Delta K^m \tag{11}$$

where K_{max} and K_{min} are the maximum and minimum SIF during the loading cycle, $R = \frac{K_{min}}{K_{max}}$ is the stress ratio, N is the number of loading cycles, and C and m are empirical material parameters.

Paris' law was initially applied just for mode-I loading. Tanaka [60] proposed a modified form of Paris' law for mixed-mode I/II fracture, as defined in equation (12).

$$\frac{da}{dN} = C\Delta K_{eqv}^m \tag{12}$$

where C and m are obtained from mode-I fatigue crack growth tests, ΔK_{eqv} is the equivalent SIF range and is a function of ΔK_I (equation (13*a*)) and ΔK_{II} (equation (13*b*)), according to equation (14).

$$\Delta K_I = K_{I,max} - K_{I,min} = (1-R)K_{I,max} \tag{13a}$$

$$\Delta K_{II} = K_{II,max} - K_{II,min} = (1-R)K_{II,max} \tag{13b}$$

$$\Delta K_{eqv} = f(\Delta K_I, \Delta K_{II}) \tag{14}$$

Different expressions of ΔK_{eqv} have been proposed in the literature and are summarized in table 3.

The fatigue cycles number (ΔN) for each finite crack length increment (Δa) is estimated by integrating equation (12), according to equation (22).

$$\int_0^{\Delta a} \frac{da}{C\Delta K_{eqv}^m} = \int_0^{\Delta N} dN = \Delta N \tag{22}$$

Then, the number of cycles ΔN_i required for the crack to grow by a very small crack increment $\Delta a_i = a_{i+1} - a_i$

is simply estimated as a function of Δa_i, according to equation (23).

$$\Delta N_i = \frac{\Delta a_i}{C(\Delta K^i_{\text{eqv}})^m} \tag{23}$$

where i is the crack growth step and ΔK^i_{eqv} is computed at the crack length a_i. Finally, the fatigue life cycle (N_f) is calculated by summing ΔN_i for each crack growth step, according to equation (24).

$$N_\text{f} = \sum_{i=1}^{n} \Delta N_i \tag{24}$$

where n is the number of crack growth steps.

The direction of crack propagation (θ_c) is equal to the initial crack orientation in the case of single fracture mode. On the other hand, three criteria are commonly used to determine θ_c under mixed-mode loading: the criterion of the maximum circumferential stress [65], the criterion of the maximum energy release rate [66], and the criterion of the minimum strain energy density [67]. In the present work, the criterion of maximum circumferential stress is adopted. The reader can refer to [56] for further details about the other two criteria.

According to the maximum circumferential stress criterion, the crack propagates in the radial direction where the circumferential stress (σ_θ) component is maximum. Then, the circumferential stress expressed in equation (6*b*) is maximized ($\frac{\partial \sigma_\theta}{\partial \theta} = 0$), according to equation (25).

$$K_\text{I} \sin\theta_\text{c} + K_\text{II}\,(3\cos\theta_\text{c} - 1) = 0 \tag{25}$$

The direction of crack propagation (θ_c) is obtained by solving equation (25), as given in equation (26) [68].

$$\theta_c = \begin{cases} 2\tan^{-1}\left[\frac{1}{4}\frac{K_\text{I}}{K_\text{II}} - \frac{1}{4}\sqrt{\left(\frac{K_\text{I}}{K_\text{II}}\right)^2 + 8}\right] & K_\text{II} > 0 \\ 2\tan^{-1}\left[\frac{1}{4}\frac{K_\text{I}}{K_\text{II}} + \frac{1}{4}\sqrt{\left(\frac{K_\text{I}}{K_\text{II}}\right)^2 + 8}\right] & K_\text{II} < 0 \end{cases} \tag{26}$$

where θ_c is positive in the anticlockwise direction with respect to the initial crack orientation direction.

2.4. Experimental setup

The change in the microstructure deflection during the fatigue loading due to crack growth in the test specimen is monitored using the optical profilometer ZoomSurf3D by Fogale Nanotech.

The central specimen fails when the pull-in phenomenon occurs, which acts as a detector of material failure and is recognized by a large variation in the measured microstructure deflection (h_2) as compared to previous cycles. Then, the occurrence of pull-in is detected at fixed time intervals during the fatigue loading in order to identify the failure of the central specimen.

Generally speaking, a fatigue loading cycle is fully characterized by the following parameters: $\sigma_{\max}$ and $\sigma_{\min}$, which are the maximum and minimum stress reached in the cycle, $\sigma_m = \frac{(\sigma_{\max}+\sigma_{\min})}{2}$ which is the mean stress, and $\sigma_a = \frac{(\sigma_{\max}-\sigma_{\min})}{2}$ which is the stress amplitude.

The fatigue load is obtained by imposing the actuation voltage between the top suspended plates and the bottom electrodes using a voltage generator. Then, the mean voltage (V_DC) and alternating (V_AC) voltage components, the stress frequency (f) and the time of actuation (t_a) need to be properly chosen during the test.

The variation of microstructure deflection caused by the stiffness degradation due to fatigue loading is monitored by applying a constant static voltage between the electrodes.

Referring to figure 6, the testing procedure is performed according to the following steps:

- The deflection of the microstructure (h_2) as a result of the static voltage (V_DC) is measured.
- The microstructure is loaded by applying the alternating (V_AC) and mean voltage (V_DC) at the chosen stress frequency (f) and for the chosen time of actuation (t_a).
- The static actuation voltage (V_DC) is applied again and the resulting microstructure deflection (h_2) is measured.

The procedure is repeated until the specimen failure, i.e. when the pull-in condition occurs due to the static voltage application.

During the fatigue loading phase, the alternating (V_AC) and mean voltage (V_DC) components are set based on the desired levels of stress amplitude and mean stress, exploiting the deflection-voltage and deflection-stress relations of the kinematic model, as explained in section 2.2.1. The stress frequency is equal to 30 kHz and 5 kHz and the time of each actuation step is equal to 1 s and 6 s, respectively.

The number of loading cycles for each step of actuation (n_i) is computed from the imposed stress frequency (f_i) and the time of actuation ($t_{a,i}$), as expressed in equation (27).

$$n_i = f_i t_{a,i} \tag{27}$$

The stress frequency f_i depends on the frequency of the applied alternating voltage (f_V). The analytical expression of the stress frequency is derived in appendix for the sake of clarity.

Finally, the number of cycles to failure (N_f) is computed according to equation (28).

$$N_f = \sum_{i=1}^{N_a} n_i \tag{28}$$

where N_a is the total number of performed actuation steps before the specimen failure.

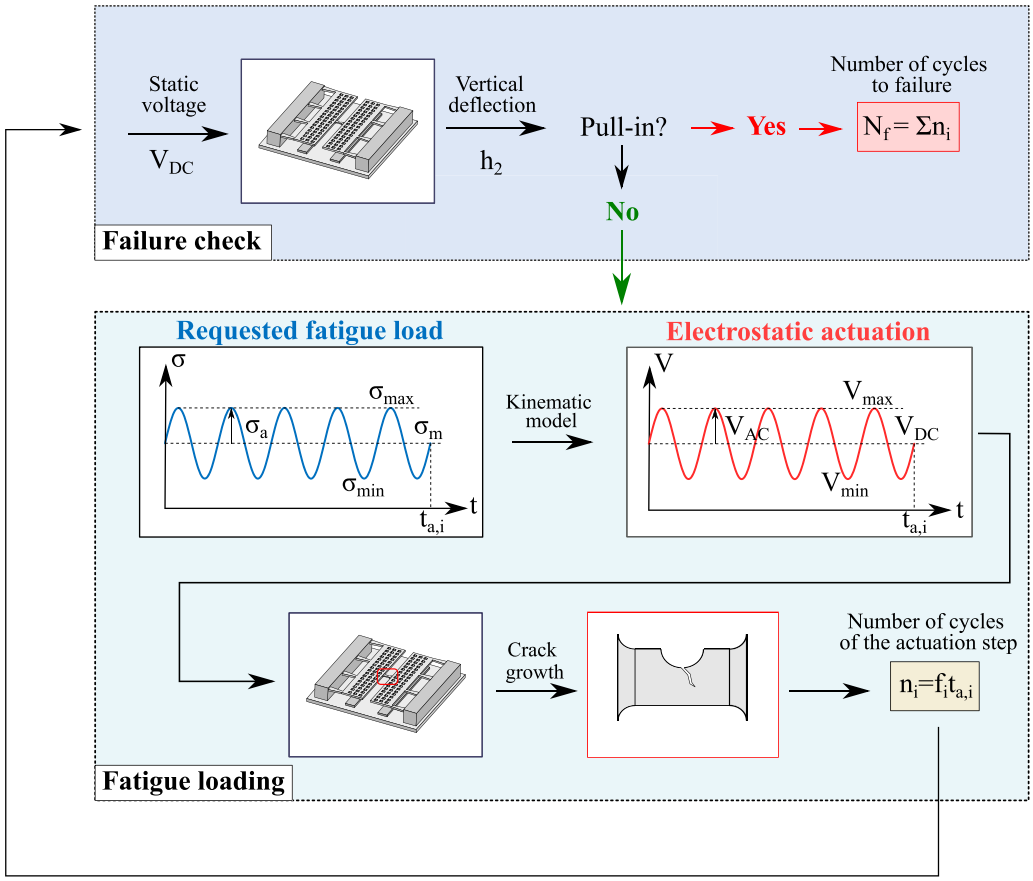

Figure 6. Scheme of procedure for the fatigue crack growth test, where V_{DC} and V_{AC} are the static and alternating voltage components respectively, σ_m and σ_a are the mean stress and stress amplitude respectively, h_2 is the measured microstructure vertical deflection, $t_{a,i}$, f_i and n_i are the time, stress frequency and number of cycles of the ith actuation step respectively, and N_f is the total number of cycles to failure.

3. FEM Model

Fatigue crack growth in the central notched specimen is simulated through a coupled-field electromechanical fracture FEM model built in Ansys.

The study of the fatigue fracture process in the proposed test specimen is a multi-physics problem, as it involves the simultaneous resolution of two coupled domains: mechanical and electrostatic. Indeed, the stress driving the crack propagation in the central specimen is caused by the electrostatic force due to the application of the voltage between the top movable plates and bottom electrodes, as explained in section 2.2.1. However, the electromechanical coupling is strongly nonlinear (as shown in equation (1)). Furthermore, fracture simulation is often high-demanding from the computational point of view, especially for three-dimensional (3D) problems.

Referring to figure 7, the procedure adopted to increase the numerical efficiency of the coupled-field electromechanical fracture simulation is described below.

- **Multiphysics FEM model of the test microstructure.** Displacement field in the central specimen as a result of the applied actuation voltage is computed from coupled electromechanical simulation of the test microstructure.
- **Fracture FEM model of the central notched specimen.** Simulation of fatigue crack growth in the central notched specimen due to the applied actuation voltage is performed according to the previously computed displacement field.
- **Paris' law.** The number of cycles to failure (N_f) is computed using the equivalent SIF range (ΔK_{eqv}) resulting from fatigue fracture simulations according to Paris' law.

Then, the modelling approach adopted in this work avoids repeating the high-demanding multiphysics simulations at each incremental crack step, as the stress and displacement fields leading to the crack growth in the central specimen are determined only once using the multiphysics FEM model of the test microstructure.

3.1. Multiphysics FEM model of the test microstructure

A coupled electromechanical FEM model of the test microstructure is built in Ansys Mechanical APDL. The optically measured dimensions reported in table 2 are used in the model. The material properties of the gold microstructure are summarized in table 4.

The FEM model of the test microstructure is shown in figure 8.

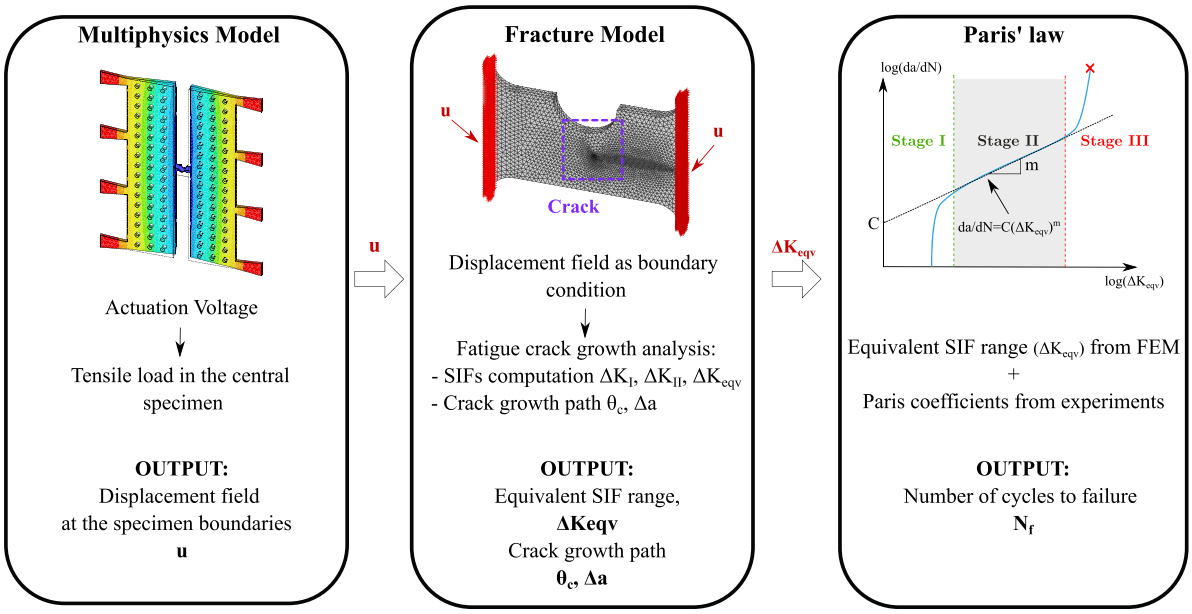

Figure 7. Steps of multiphysics fatigue fracture model.

Table 4. Material properties of the gold layer of the test microstructure.

Property	Symbol	Value	Unit	References
Young modulus	E	98.5	MPa	[69]
Poisson ratio	ν	0.42	—	[48, 69]
Density	ρ	$19.32 \cdot 10^{15}$	$\mathrm{kg} \cdot \mu\mathrm{m}^{-1}$	[48, 69]
Yield stress	σ_y	110	MPa	[47]

The test microstructure is modelled as a 3D solid structure using tetrahedral 10-node SOLID186 elements with three degrees-of-freedoms (DOFs) per node, namely displacement in x (u_x), y (u_y) and z (u_z) directions. A sufficiently refined mesh is used near the notch region to correctly describe stress and strain distributions. All DOFs at the end of trapezoidal beams are fixed (figure 8(a)).

The electromechanical coupling is modelled using reduced-order one-dimensional (1D) TRANS126 elements. The TRANS126 element is a plane capacitor modelling the capacitive response of an electromechanical device as a function of displacement in one direction. The element has two nodes, connecting the nodes of the FE model between which the electrostatic force acts. Each node has two DOFs: the structural displacement (u_x, u_y, or u_z) and the electrostatic voltage (V).

TRANS126 elements connect the nodes of the top movable plates and those nodes representing the bottom fixed electrodes, which are not directly included in the FEM model as they are described by boundary conditions at TRANS126 element nodes (figures 8(b) and (c)).

The electrostatic field fringing effect is neglected, and then the capacitance C of electrodes modelled by TRANS126 elements depends on the gap g between electrodes (equation (29)), which is a function of the displacement of the top plates (h_2).

$$C = \frac{\varepsilon_0 A}{g(h_2)} \tag{29}$$

The set of TRANS126 elements is generated automatically in Ansys using the command EMTGEN (figures 8(b) and (c)), which also automatically creates the plane of nodes representing the bottom fixed electrodes.

The electrostatic voltage is applied on the TRANS126 nodes connected to the top plates mesh, on the other hand, the electrostatic voltage and the translational DOFs of the bottom electrodes nodes are set to zero.

Just SIFs corresponding to the maximum load, i.e. $K_{\mathrm{I,max}}$ and $K_{\mathrm{II,max}}$, are required for the fatigue crack growth computation, according to equations (13) and (14) as the compression phase can be neglected. Then, multiphysics simulations are carried out at the maximum voltage $V_{\max}$ causing the maximum stress level ($\sigma_{\max}$) in the specimen during the cycle.

Finally, displacements of nodes at the edges of the central specimen are saved for the following fatigue crack growth analysis.

3.2. *Fracture FEM model of central notched specimen model*

A 3D model of the central notched specimen with a pre-existing sharp crack at the notch root is built in Ansys for the fatigue crack growth analysis, assuming the initial crack length (a_0) and orientation (θ_0), as shown in figure 9.

The specimen material is considered linear elastic and isotropic, i.e. plastic effects do not cause damage in the gold material and LEFM hypotheses hold. This is quite reasonable because the maximum actuation voltage during cycling does not exceed 140 V, then the stress at the notch region is below the yield limit, as it will be demonstrated in section 4.1.

The fracture analysis is performed just modelling the notched specimen. Then, the mesh of the model is composed of SOLID186 structural elements, and no multiphysics

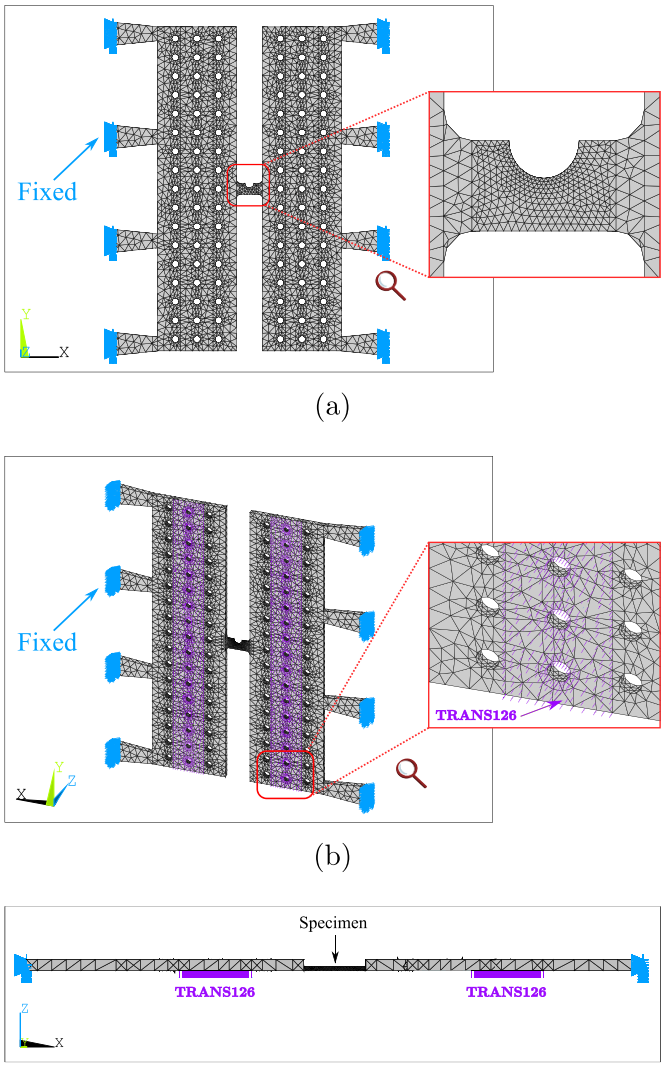

Figure 8. Multiphysics FEM model of test microstructure for coupled electromechanical analysis. (a) 3D structural mesh composed of SOLID186 elements (represented in grey), with detail of the central notched specimen. (b) Set of TRANS126 elements (represented in purple), with detail of the bottom view. (c) Side view of the test microstructure.

elements are included in the model. Displacement field of the nodes at the edges of the specimen is computed with the multiphysics model described in section 3.1 and is applied as boundary conditions.

Referring to figure 10, the mesh of the model is built according to the procedure summarized below.

- The 3D volume of the central notched specimen with a pre-existent crack is generated and a cylindrical volume around the crack tip is created to control the mesh generation near the crack region (figure 10(a)).
- Collapsed quarter-point singular elements are used to accurately estimate the singularity in the stress field near the crack tip [70]. Singular elements are obtained by collapsing the 20-node brick version of SOLID186 elements (figure 10(f)). A spider web mesh made of 4 concentric rings is created on both faces of the cylindrical volume using 2D MESH200 elements to simplify the generation of singular elements. The mesh of these areas will provide the pattern for the solid elements mesh within the cylindrical volume. The innermost ring is composed of 24 2D singular elements automatically generated by the KSCON command in Ansys, on the other hand, the remaining rings are meshed using 8-node quadrilateral elements (figure 10(b)).
- One of the two meshed areas of the cylindrical volume is defined as the source, the other one as the target. Then, the cylindrical volume is meshed by sweeping the mesh pattern of the source to the target area along the specimen thickness (figure 10(c)).
- The rest of the model is meshed using 10-node tetrahedral version of SOLID186 elements. The mesh size is refined near the crack front, on the other hand, the size gradually increases when moving away from the crack (figures 10(d)–(f)).

The update of geometry and mesh is one of the main issues when dealing with crack propagation with FEM, especially in 3D models. However, the strategy previously described allows for automatic remeshing during the simulation based on the location of the crack tip.

The crack path is determined by computing the direction of crack propagation (θ_c) at each crack growth step, considering a fixed crack length increment (Δa). The mixed-mode SIFs $K_{\mathrm{I,max}}$ and $K_{\mathrm{II,max}}$ are computed in Ansys from the interaction energy integral using the built-in CINT command and the crack propagation direction (θ_c) is determined from equation (25). Then, the equivalent SIF range (ΔK_{eqv}) is computed according to equations (16) and (17), and the number of cycles (ΔN) required for the crack to grow by Δa is obtained from equation (23).

Then, the mesh of the model is removed, the geometry of the model is updated according to the new crack tip position, quarter-point singular elements are created around the new crack tip and a new mesh is generated in the remaining unmeshed volume, following the strategy described above. Finally, the same procedure is repeated for the next crack growth steps, until the crack reaches one of the specimen edges.

4. Results and discussion

The results of the kinematic and multiphysics FEM-based models of the test microstructure, as well as the results of the fatigue crack growth analysis are presented in this section. Then, a comparison between the fatigue crack path in the central notched specimen resulting from the fracture model and measured experimentally with SEM after the specimen failure is performed. Finally, the number of cycles to failure computed

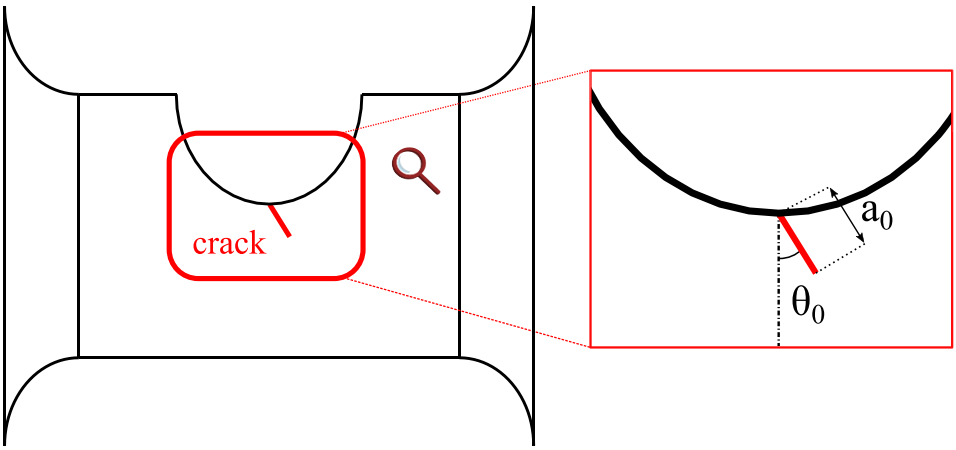

Figure 9. Schematic of the initial crack at the notch root, where a_0 and θ_0 are the initial crack length and orientation, respectively.

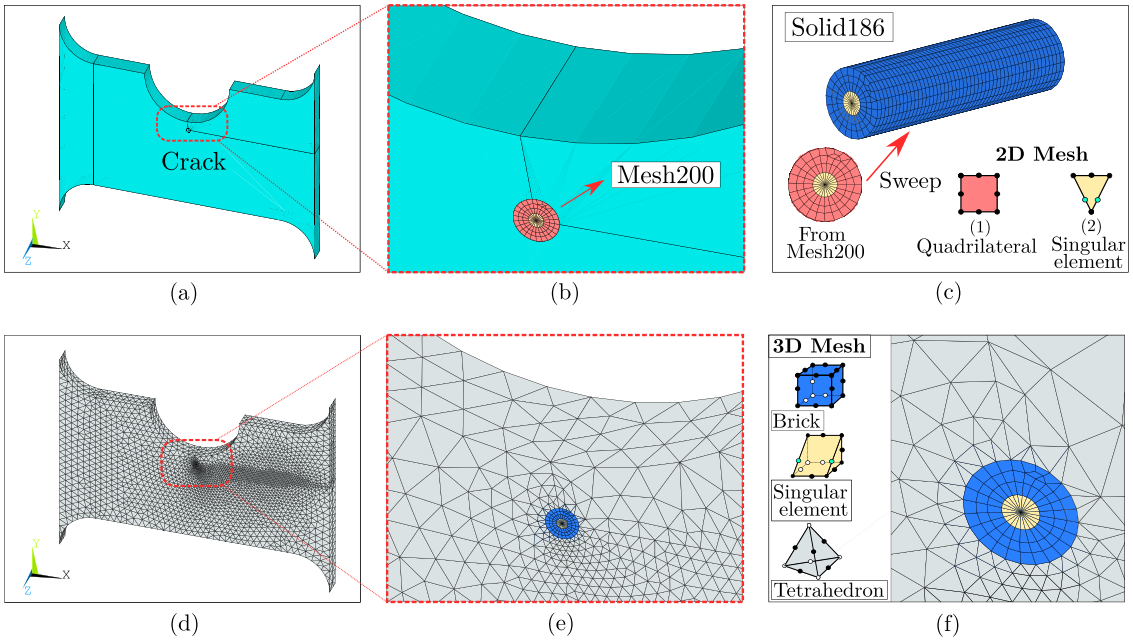

Figure 10. The 3D FEM model of the central notched specimen with a pre-existent crack at the notch root. (a) Volume of the specimen with detail of (b) cylindrical volume created around the crack tip, (c) elements breakdown of the cylindrical volume with spider web mesh pattern used to create the volume mesh, (d) meshed FEM model with detail of (e)–(f) crack region, where 20-node brick, 15-node collapsed singular and 10-node tetrahedral elements are represented in blue, yellow and grey, respectively.

using Paris' law is validated by the fatigue life data from experimental tests.

4.1. Multiphysics FEM simulation of the test microstructure

Figure 11 shows the distribution of the out-of-plane displacement and Von Mises stress in the test microstructure obtained from the multiphysics FEM model built in Ansys considering a static voltage of 140 V.

The stress in the movable plates and trapezoidal beams is much lower than in the central specimen. Then, the notch root on the bottom surface of the central specimen is the most stressed region, whereas further from the notch the highest stress occurs in the material region at an angle of 45° to the line connecting the notch root to the centre of the specimen, as confirmed by figures 11(b) and (c). In addition, although the stress increases near the connection between the specimen and movable plates, then the increase in stress is quite small and does not alter the stress distribution in the specimen thanks to the inclusion of rounded corners in the microstructure design.

The curves of the microstructure vertical deflection (h_2) and the maximum Von Mises stress at the notch root obtained by applying a static voltage (V_{DC}) ranging 0–140 V are shown in figures 12(a) and (b), respectively. The static voltage is such

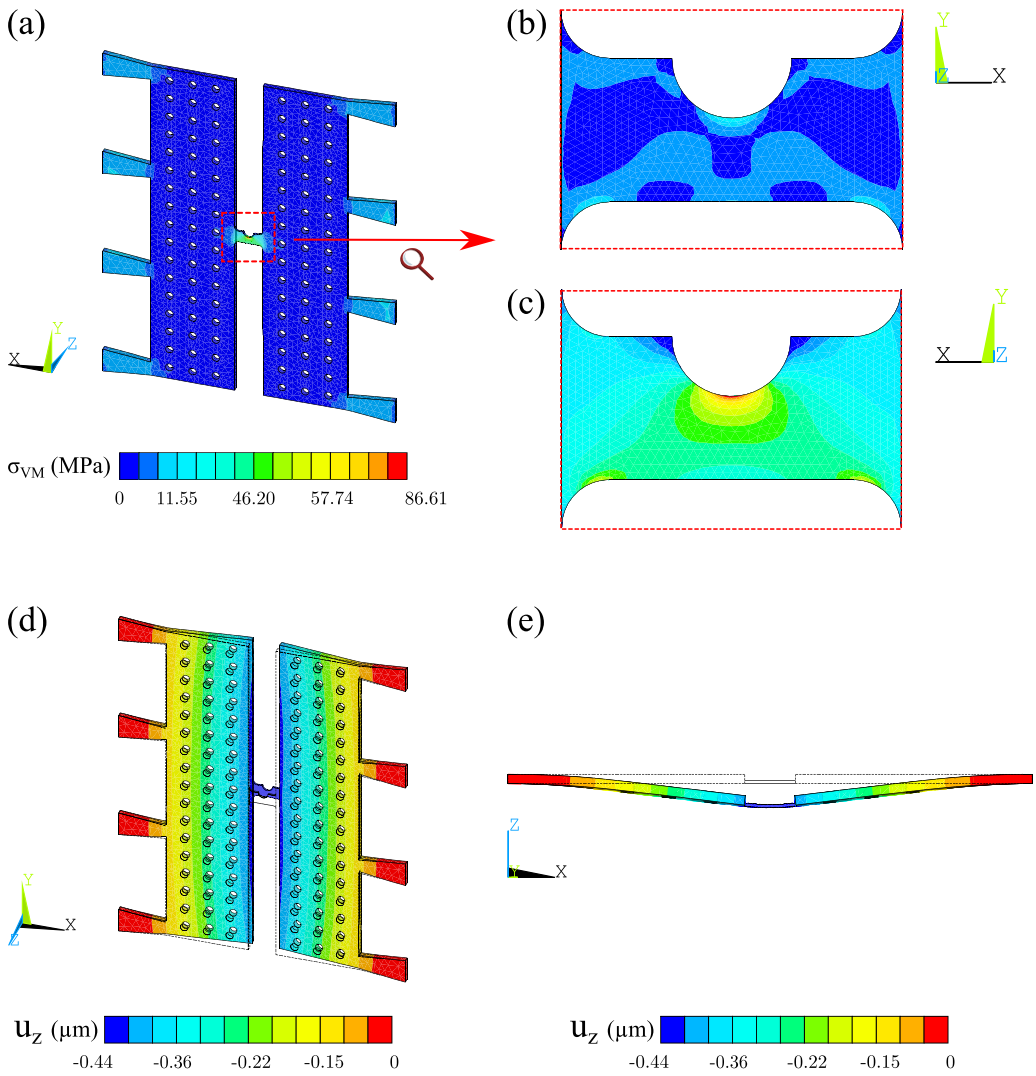

Figure 11. Multiphysics FEM simulation results of test microstructure actuated by a static voltage (V_{DC}) of 140 V. (a) Von Mises stress distribution (σ_{VM}), with detail of (b) top surface and (c) bottom surface of the central specimen. Out-of-plane displacement distribution (u_z), with (d) isometric view (scale: 30) and (e) lateral view (scale: 30).

that the pull-in phenomenon does not occur and the maximum Von Mises stress at the notch does not overcome the yield stress of the gold material (table 3), as also demonstrated in previous works [47]. Then, the material behaviour in the central specimen is elastic in the voltage range $0-140$ V, and LEFM assumptions hold.

The kinematic model of the test microstructure proposed in section 2.2.1 is validated using the FEM-based model in Ansys.

The deflection of the test microstructure (h_2) due to the applied static voltage (V_{DC}) computed through the multiphysics FEM model is used in the kinematic model. Then, the nominal axial stress ($\sigma_{a,nom}$) is computed using equations (2) and (3) and the maximum stress ($\sigma_{n,max}$) at the notch root is computed using equation (4).

Figure 13 shows the comparison between axial stress values computed using FEM and kinematic models.

The good correspondence between the stress values demonstrates that the deflection of the microstructure can be correlated to the stress in the central notched specimen. Then, the variation in the microstructure deflection when actuated by static voltage can be properly used as a detector of the variation in the device stiffness caused by the crack growth in the central specimen during the fatigue loading test.

4.2. Fatigue fracture simulation of central notched specimen

The fatigue fracture analysis aims to determine the crack propagation path in the central notched specimen when alternating voltage actuates the test microstructure, causing a fatigue load in the central specimen.

Cracks preferentially nucleate at defects acting as local stress and strain raisers, then several crack nucleation sites may exist across the specimen surface [33]. Fabrication processes, etching techniques, and substrate materials greatly affect the occurrence of initial defects, then a variation may exist from sample to sample. However, cracks are much more likely to start at the notch root, which is the most stressed

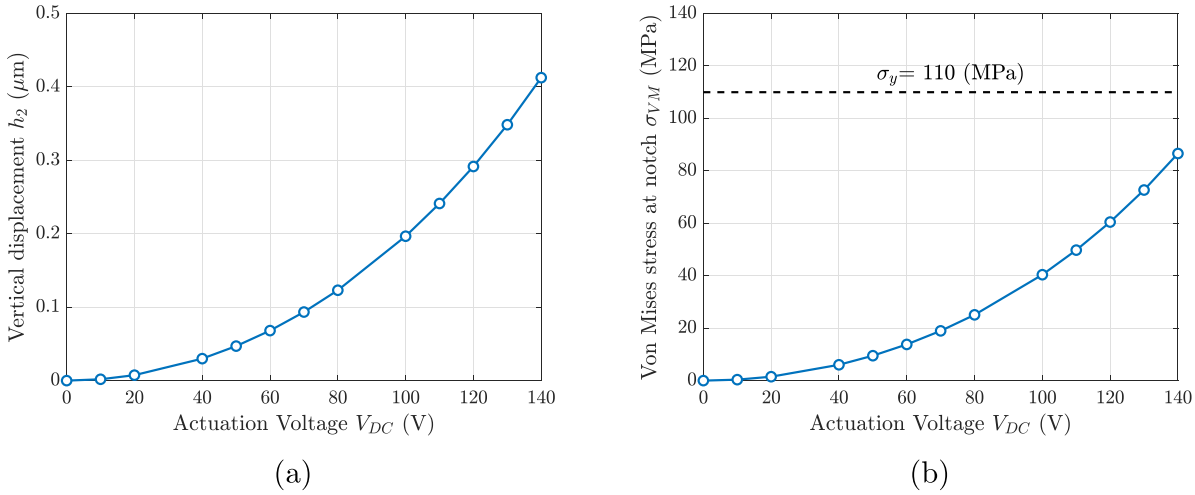

Figure 12. Curves of (a) vertical deflection of the test microstructure (h_2) and (b) maximum Von Mises stress (σ_{VM}) at the notch root, obtained from the multiphysics FEM model with static voltage (V_{DC}) ranging 0–140 V.

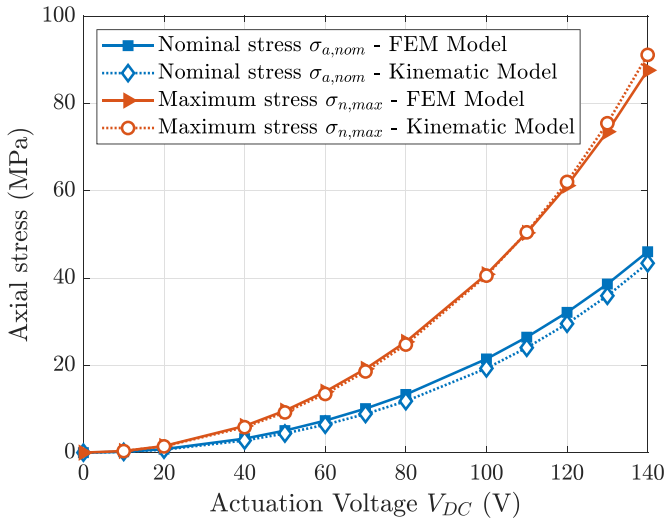

Figure 13. Comparison between nominal axial stress ($\sigma_{\mathrm{a,nom}}$) and the maximum axial stress at the notch root ($\sigma_{\mathrm{n,max}}$) obtained with the FEM (solid lines) and kinematic (dashed lines) models.

region in the specimen, as also demonstrated by FEM simulation results reported in section 4.1. Furthermore, different samples are inspected by SEM after some fatigue cycles (figure 14), confirming that the notch fosters crack propagation, despite the differences between samples.

The fatigue crack propagation due to the applied electrostatic voltage is simulated through the fracture FEM model built in Ansys. The crack path is determined following the procedure described in section 3.2 and the crack propagation angle (θ_c) is computed according to equation (26), using the mixed-modes SIFs (K_{I} and K_{II}) evaluated at the specimen bottom surface, which is the most stressed area.

Figure 15 shows the sequence of crack evolution during fatigue cycling at the alternating voltage of 140 V, and null mean voltage. The results show that the developed model is able to simulate the propagation of the crack, which grows following the direction of maximum tangential stress (as predicted by the LEFM theory), until it reaches the external edge of the specimen, causing the final failure of the microstructure.

Crack propagation in the central specimen may be affected by the initial crack length and orientation, which may depend on the microstructure of the gold material ahead of the notch root. Since the crack nucleation phase is not analyzed in this work, then a sensitivity analysis is performed to evaluate the influence of the assumed initial crack length and orientation on the resulting crack propagation path. The influence of the chosen crack incremental length (Δa) is analyzed as well.

A comparison between the crack paths obtained varying the initial crack length and orientation, considering a fixed crack increment (Δa) of 0.5 μm during cycling, is shown in figures 16(a) and (b) respectively. In the former, the initial crack orientation (θ_0) is 10°, in the latter the initial crack length (a_0) is 1 μm. The results demonstrate that the crack path is little affected by the initial crack length and orientation.

Figure 16(c) shows the variation of crack paths with different crack incremental lengths, considering initial crack length (a_0) of 0.5 μm and initial crack orientation (θ_0) of 10°. The crack paths are similar as long as the crack incremental length is quite small, i.e Δa is smaller than 1 μm, on the other hand, the crack path is slightly different for larger incremental length, i.e. $\Delta a = 2$ μm.

4.3. *Experimental results and discussion*

The crack propagation path is experimentally observed by SEM, inspecting the central specimen just after failure, i.e. when the pull-in phenomenon occurs, as explained in section 2.4.

Figure 17 shows the SEM images of two specimens after failure at different magnifications. The specimens were cycled at the alternating voltage of 140 V and null mean voltage, with

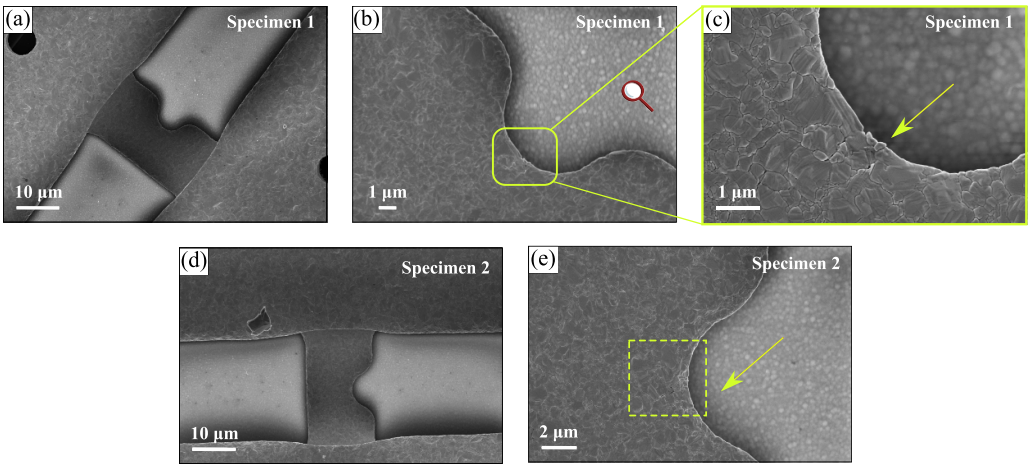

Figure 14. SEM images of notched specimens. (a) Specimen 1 and (d) specimen 2 before fatigue cycling. Crack nucleation at the notch root region of (b)–(c) specimen 1 and (e) specimen 2.

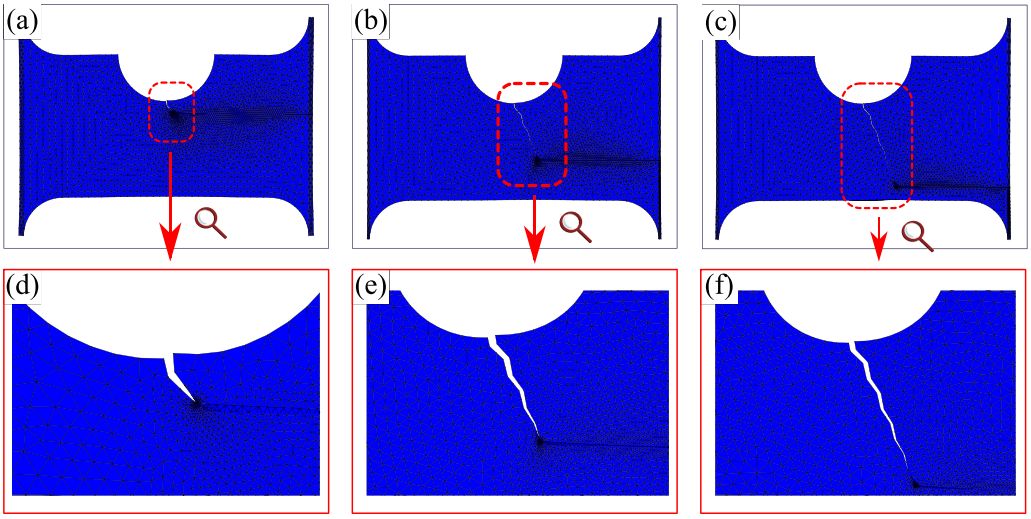

Figure 15. Evolution of crack path during fatigue cycling caused by alternating voltage of 140 V, and null mean voltage.

the stress frequency and total time of actuation equal to 30 kHz and 10 s, respectively ($N_f = 300\,000$).

The SEM images show that failure occurs due to crack propagation from the notch root in the central specimen, as pointed out by the green arrows in figures 17(b) and (g). Furthermore, the crack propagation path in the two specimens is very similar, as evidenced by comparing figures 17(c) and (h), although the crack initiation site in the two specimens is slightly different, as resulting by comparing figures 17(d) and (j). This is because crack nucleation is influenced by the local variation in grain morphology as well as by the local defects distribution in the region ahead of the notch, which may vary among the two specimens (figures 17(e) and (k)).

Then, different morphologies of the material ahead of the notch may be responsible for different initial crack paths, but once the crack initiates, it propagates following the direction of maximum principal stress according to LEFM theory.

Figure 18 shows a comparison between the crack propagation path resulting from the fracture model (a_0, θ_0 and Δa are equal to 0.5 μm, 10° and 0.4 μm, respectively) and measured experimentally. The slight deviation between the two crack paths, highlighted in green in figure 18(a), can be attributed to local defects present in the material, locally influencing the crack path. Nevertheless, the consistency of the experimental and simulated crack paths is quite good, confirming the validity of LEFM theory in characterizing the fatigue fracture behaviour of microstructures, as well as the effectiveness of the built FEM model in predicting crack growth in the notched specimen, even at micro-scale.

The number of cycles to failure (N_f) in the central specimen can be computed using Paris' law reported in equation (11), exploiting the results of fatigue fracture FEM simulations.

Paris' law is a function of empirical material coefficients C and m. However, values of C and m coefficients for the thin film gold material are not available in the literature as far as

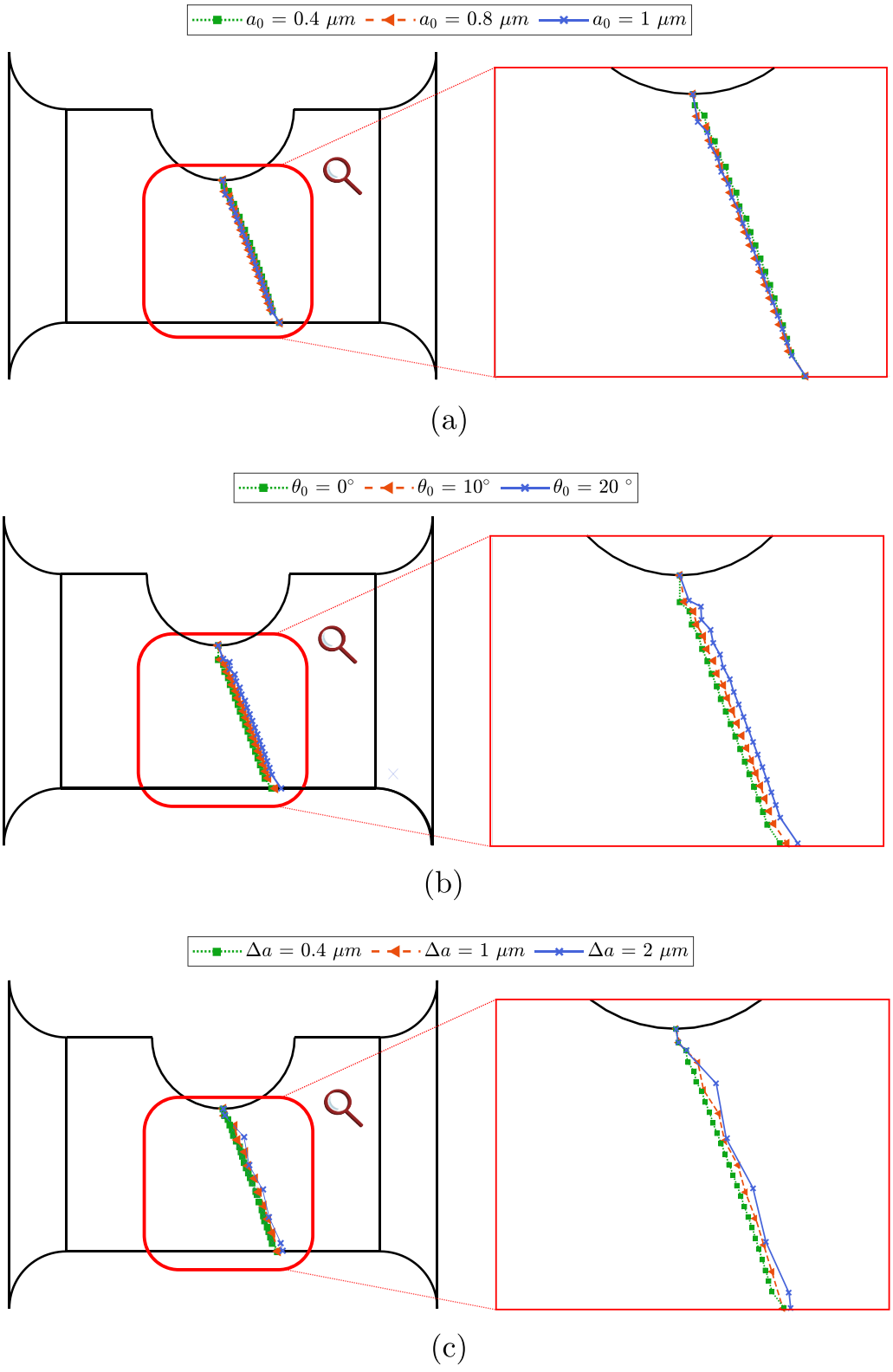

Figure 16. Influence of the initial crack length (a_0), orientation (θ_0) and crack incremental length (Δa) on crack propagation path, considering an alternating voltage of 140 V and a null mean voltage during cycling. (a) Variation of initial crack length (a_0), with initial crack orientation (θ_0) of 10° and crack incremental length (Δa) of 0.5 μm. (b) Variation of initial crack orientation (θ_0) with initial crack length (a_0) of 1 μm and crack incremental length (Δa) of 0.5 μm. (c) Variation of crack incremental length with initial crack length (a_0) of 0.5 μm and initial crack orientation (θ_0) of 10°.

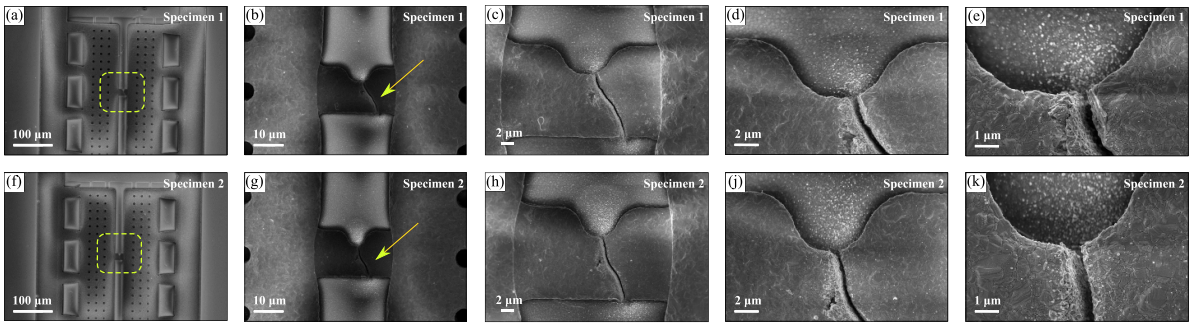

Figure 17. SEM images at different magnifications showing the central specimen after failure. The alternating voltage is 140 V, the mean voltage is null, the stress frequency is 30 kHz and the time of actuation is 10 s ($N_f = 300000$). (a)–(e) Specimen 1 and (f)–(k) Specimen 2, with the green arrow pointing to the crack.

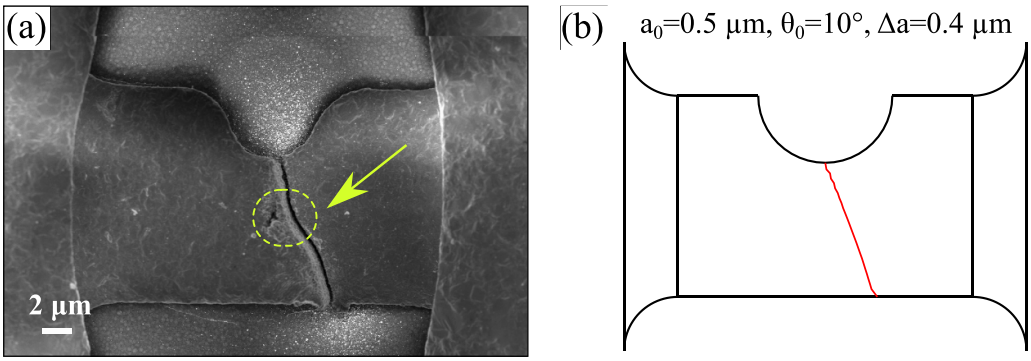

Figure 18. Comparison between (a) experimental and (b) simulation results (a_0, θ_0 and Δa are equal to 0.5 μm, 10° and 0.4 μm, respectively) of crack propagation path in specimen 2. The specimen is actuated by alternating voltage of 140 V, null mean voltage, with stress frequency of 30 kHz and time of actuation of 10 s ($N_f = 300000$).

the authors know. Moreover, C and m coefficients are usually determined by monitoring the crack increment during the fatigue cycling, which was not carried out in this work as the specimen was inspected by SEM just at failure. Indeed, only the number of cycles to failure (N_f) corresponding to different alternating voltages (V_{AC}) is recorded during experiments.

Nevertheless, C and m are estimated by minimizing the error between the number of cycles to failure obtained from experimental measurements ($N_{f,exp}$) and computed using equations (23) and (24), according to equation (30).

$$\min \left\{ \sum_{j=1}^{N_m} \left(N_{f,exp}^{j} - \sum_{i=1}^{n} \frac{\Delta a_i^j}{C(\Delta K_{eqv,i}^j)^m} \right)^2 \right\} \qquad (30)$$

where N_m is the number of experimental measurements. The equivalent SIF range ($\Delta K_{eqv,i}$) in equation (30) is computed at each crack length increment using the FEM fracture model, considering a crack incremental length (Δa) of 0.4 μm, an initial crack length (a_0) and orientation (θ_0) equal to 0.5 μm and 10°, respectively. The experimental number of cycles to failure $N_{f,exp}$ is measured at different alternating voltage amplitude (V_{AC}) with the stress frequency of 5 kHz.

The results of Paris' law coefficients estimation, based on Tanaka's (equation (16)) and Irwin's (equation (17)) models, are reported in table 5. The results show that the values of C and m coefficients obtained from Tanaka's and Irwin's models are similar.

The values of Paris' coefficients computed using equation (30) are compared to those obtained from micro-scale experimental fatigue tests performed on some common materials for MEMS devices, such as Polysilicon, LIGA Nickel, and Tungsten, as reported in table 6.

The comparison between the values of m exponent, which do not depend on the load ratio R, shows that the estimated exponent m for thin film gold material is quite reasonable, as it is in the same range as LIGA Nickel and Tungsten materials.

Table 6 also shows the Paris' coefficients values of metallic materials obtained from experimental tests on macro-size specimens. The comparison shows slight variability among the results, demonstrating that the specimen size, as well as the material composition and microstructure, influence the values of Paris' law coefficients. Furthermore, there is a slight difference between experimental results obtained from macro-scale and micro-scale tests, which was also evidenced by Gabel *et al* [20]. Despite this, the values of exponents m are in the same order of magnitude, which demonstrates the comparability between macroscopic and microscopic tests, as well as the validity of Paris' law and LEFM theory in describing the fatigue fracture behaviour of materials at micro-scale.

Table 5. Results of Paris' law coefficients estimation.

Δa (μm)	Alternating Voltage V_{AC}	Experimental fatigue life $N_{f,exp}$	Simulations fatigue life $N_{f,sim}$	Error (%)
Tanaka's model (equation (16))			$C = 2.61\ 10^{-10}$, $m = 1.96$	
0.4	120 (V)	270 000	271 020	−0.38
	140 (V)	150 000	148 870	−0.75
Irwin's model (equation (17))			$C = 5.68\ 10^{-10}$, $m = 1.95$	
0.4	120 (V)	270 000	268 570	−0.53
	140 (V)	150 000	155 560	3.71

Table 6. Paris' coefficients of the most common materials used in MEMS devices and metallic materials obtained from macroscopic tests.

Material	Scale	Young modulus (GPa)	C[a]	m
Gold (Tanaka's model)	Micro-scale	98	$2.61\ 10^{-10}$	1.96
Gold (Irwin's model)	Micro-scale	98	$5.68\ 10^{-10}$	1.95
Gold	Macro-scale	88 [71]	$8.41\ 10^{-12}$ [71]	3.5 [71]
Aluminum	Micro-scale	55–81 [72]	$5.0\ 10^{-12}$ [73]	4.4 [73]
Aluminum	Macro-scale	70	$3.92\ 10^{-11}$ [74]	3.7 [74]
Titanium	Micro-scale	260–350 [75]	$2.55\ 10^{-13}$ [76]	5.0 [76]
Titanium	Macro-scale	120	$9.56\ 10^{-12}$ [74]	3.8 [74]
Polysilicon	Micro-scale	164 [77]	$1.15\ 10^{-14}$ [78]	26.9 [78]
LIGA nickel	Micro-scale	180 [38]	$3.98\ 10^{-14}$ [38]	2.2 [38]
Tungsten	Micro-scale	670–710 [79]	$6.70\ 10^{-12}$ [20]	4.3 [20]
Tungsten	Macro-scale	410	$5.2\ 10^{-12}$ [80]	2.8 [80]

[a] $\frac{da}{dN}$ in (m/cycle), ΔK in (MPa $\cdot$ $m^{1/2}$)

5. Conclusions

The fatigue fracture characterization of MEMS gold-based notched specimens subjected to cyclic loading is presented in this work.

On-chip fatigue tests are performed using a test microstructure specifically designed to load the specimen at different stress levels and with multiple loading cycles using electrostatic actuation. Numerical simulations of fatigue crack growth are performed using a coupled-field electromechanical fracture finite element model, on the basis of LEFM theory and Paris' law.

A kinematic model of the test microstructure is derived and the axial stress in the central specimen is computed through the measured microstructure deflection caused by the actuation voltage. Then, the variation in the microstructure deflection after the fatigue loading is correlated to the stiffness degradation of the central specimen due to crack propagation. The central specimen is not inspected when loaded thanks to the developed test microstructure design, and the specimen failure is identified by the instantaneous large variation in the microstructure deflection, as the pull-in condition occurs when the specimen fractures.

SEM analyses of specimens after failure confirm that cracks start at the notch root, which acts as local stress and strain raiser fostering crack propagation. Furthermore, the comparison between the crack propagation path resulting from SEM images and obtained from the fracture model shows a good agreement, with the slight deviation being attributed to local defects present in the material which can locally influence the crack path. This confirms the validity of the LEFM theory in characterizing the fatigue fracture behaviour of microstructures, as well as the effectiveness of the developed fracture model in predicting crack growth in micro-size samples.

Finally, Paris' law is applied to compute the fatigue life by exploiting the results of the fracture FEM model. Paris' coefficients are estimated by minimizing the error between the number of cycles to failure obtained from experimental measurements and numerically computed, as paris' coefficients are not available in the literature for the thin film gold material. The results are quite reasonable if compared to Paris' law coefficients obtained from fatigue tests on micro-size samples and from macroscopic tests on the most common metallic materials. Then, this further demonstrates the reliability of the developed fracture model and experimental measurements.

Data availability statement

All data that support the findings of this study are included within the article (and any supplementary files).

Appendix. Stress frequency computation

The application of the actuation voltage V between fixed and moving electrodes causes the electrostatic force F_{e} according to equation (A.1).

$$F_{\mathrm{e}}(t) = \frac{\varepsilon_0 A V^2}{2(g_0 - z)^2} \tag{A.1}$$

where ε_0 is the permittivity, $A = l_{\mathrm{e}} w_e$ is the overlap area, l_{e} and w_{e} are the length and width of the bottom electrode respectively, g_0 is the initial air gap thickness, z is the displacement of the moving electrode. The actuation voltage V is expressed by equation (A.2).

$$V(t) = V_{\mathrm{DC}} + V_{\mathrm{AC}} \sin(f_V t) \tag{A.2}$$

where V_{DC} is the mean voltage component, V_{AC} is the amplitude of the alternate component, and f_V is the frequency of the electric actuation. The electrostatic force generated by the actuation voltage reported in equation (A.2) is expressed according to equation (A.3).

$$F_e(t) = \frac{\varepsilon_0 A \left[V_{\mathrm{DC}} + V_{\mathrm{AC}} \sin(f_V t)\right]^2}{2(g_0 - z)^2} \tag{A.3}$$

Equation (A.3) is rewritten according to equation (A.4) using the trigonometric relation $\sin^2(f_V t) = \left[1 - \cos(2 f_V t)\right]^2 / 2$ [81].

$$F_e(t) = A + B \sin f_V t + C \cos(2 f_V t) \tag{A.4}$$

where the coefficients A, B and C are reported in equations (A.5*a*)–(A.5*c*) respectively.

$$A = \frac{\varepsilon_0 A}{(g_0 - z)^2} \left[\frac{1}{2} V_{\mathrm{DC}}^2 + \frac{1}{2} V_{\mathrm{AC}}^2\right] \tag{A.5a}$$

$$B = \frac{\varepsilon_0 A}{(g_0 - z)^2} V_{\mathrm{DC}} V_{\mathrm{AC}} \tag{A.5b}$$

$$C = \frac{\varepsilon_0 A}{4(g_0 - z)^2} V_{\mathrm{AC}}^2. \tag{A.5c}$$

Equation (A.4) shows that the electrostatic force loading the structure is the superimposition of two harmonic components, one at the frequency f_V, and one at the frequency $2 f_V$.

The frequency of the electrostatic force is twice the electric frequency ($f = 2 f_V$) if the static voltage component is null ($V_{\mathrm{DC}} = 0$), as $B = 0$ according to equation (A.5*b*).

Symbols

F_e	Electrostatic force
ε_0	Permittivity
A	Overlap area
g	Air gap thickness
h_1	Deflection at the centre of the top plate
l_s	Specimen length
w_s	Specimen width
t_s	Specimen thickness
r_c	Specimen to plate connection radius
r_n	Notch root radius
l_p	Actuation plate length
w_p	Actuation plate width
t_p	Actuation plate thickness
l_b	Flexural beam length
w_{bi}	Flexural beam internal width
w_{be}	Flexural beam external width
t_b	Flexural beam thickness
l_e	Lower electrode length
w_e	Lower electrode width
t_e	Lower electrode thickness
V	Actuation voltage
α	Rotation angle of top suspended plate
Δl	Total horizontal elongation of the specimen
h_2	Deflection at the edge of the top plate
P	Axial force
M	Bending moment
E	Young modulus
A_s	Specimen cross section
J	Bending moment of inertia
z_s	Coordinate along specimen thickness
σ_a	Axial stress
$\sigma_{a,P}$	Axial stress due to axial force
$\sigma_{a,M}$	Axial stress due to bending moment
K_t	Elastic stress concentration factor
$\sigma_{n,max}$	Maximum stress at the notch root
θ	Polar coordinate in crack reference frame
r	Radial coordinate in crack reference frame
f_{ij}	Dimensionless shape function
K_i	Mode-i stress intensity factor
ν	Poisson ratio
G_i	Mode-i energy release rate
μ	Shear modulus
γ_{el}	Elastic strain energy density
u	Displacement
x	Cartesian coordinate
y	Cartesian coordinate
n_j	Normal vector
t_j	Traction vector
ΔK_i	Stress intensity factor range
R	Stress ratio
N	Number of loading cycles
C	Paris coefficient
m	Paris coefficient
ΔK_{eqv}	Equivalent SIF range
Δa	Crack length increment
a	Crack length
N_f	Fatigue life cycle
θ_c	Crack propagation direction
σ_m	Mean stress of fatigue cycle
σ_a	Stress amplitude of fatigue cycle

V_{AC}	Alternating voltage
V_{DC}	Mean voltage
t_a	Time of actuation
f	Stress frequency
f_V	Electric frequency

Acronyms

MEMS	Micro-electro-mechanical system
SEM	Scanning electron microscope
FEM	Finite element method
XFEM	Extended finite element method
LEFM	Liner elastic fracture mechanics
CZM	Cohesive zone model
PFM	Phase-field model
SIF	Stress intensity factor
DOD	Degree-of-freedom

Subscripts

max	Maximum
min	Minimum
0	Initial

ORCID iDs

Francesca Pistorio https://orcid.org/0000-0001-5945-7257
Aurelio Somà https://orcid.org/0000-0002-1111-3305

References

[1] Bryzek J 1996 *Sens. Actuators* A **56** 1–9
[2] Pattanaik P and Ojha M 2021 *Mater. Today* **81** 224–6
[3] Khoshnoud F and de Silva C W 2012 *IEEE Instrum. Meas. Mag.* **15** 14–24
[4] Zhu J, Liu X, Shi Q, He T, Sun Z, Guo X, Liu W, Sulaiman O B, Dong B and Lee C 2019 *Micromachines* **11** 7
[5] Ghazali F A M, Hasan M N, Rehman T, Nafea M, Ali M S M and Takahata K 2020 *J. Micromech. Microeng.* **30** 073001
[6] Choudhary V and Iniewski K 2017 *Mems: Fundamental Technology and Applications* (Boca Raton, FL: CRC Press)
[7] Lammel G 2015 The future of mems sensors in our connected world *2015 28th IEEE International Conference on Micro Electro Mechanical Systems (MEMS) (Estoril, Portugal, 2015)* pp 61–64
[8] Bhatt G, Manoharan K, Chauhan P S and Bhattacharya S 2019 *Sensors for Automotive and Aerospace Applications* (Berlin: Springer) pp 223–39
[9] Javed Y, Mansoor M and Shah I A 2019 *Sens. Rev.* **39** 652–64
[10] Pistorio F, Saleem M M and Somà A 2021 *Appl. Sci.* **11** 1129
[11] Le X, Shi Q, Vachon P, Ng E J and Lee C 2021 *J. Micromech. Microeng.* **32** 014005
[12] Haroun A, Le X, Gao S, Dong B, He T, Zhang Z, Wen F, Xu S and Lee C 2021 *Nano Express* **2** 022005
[13] Tilli M, Paulasto-Krockel M, Petzold M, Theuss H, Motooka T and Lindroos V 2020 *Handbook of Silicon Based Mems Materials and Technologies* (Amsterdam: Elsevier)
[14] Huang Y, Vasan A S S, Doraiswami R, Osterman M and Pecht M 2012 *IEEE Trans. Device Mater. Reliab.* **12** 482–93
[15] Ando T, Shikida M and Sato K 2001 *Sens. Actuators* A **93** 70–75
[16] Maligno A, Whalley D C and Silberschmidt V V 2012 *Microelectron. Reliab.* **52** 1665–78
[17] Zhang Y, Wu K, Li H, Shen S, Cao W, Li F and Han J 2022 *Microelectron. Reliab.* **139** 114829
[18] Langfelder G, Dellea S, Zaraga F, Cucchi D and Urquia M A 2011 *IEEE Trans. Ind. Electron.* **59** 4938–48
[19] Hardwick D 1987 *Thin Solid Films* **154** 109–24
[20] Gabel S, Merle B, Bitzek E and Göken M 2022 *J. Mater. Res.* **37** 2061–72
[21] Gu X W, Wu Z, Zhang Y-W, Srolovitz D J and Greer J R 2013 *Nano Lett.* **13** 5703–9
[22] Kumar S, Haque M and Gao H 2009 *Appl. Phys. Lett.* **94** 253104
[23] Kumar S, Li X, Haque A and Gao H 2011 *Nano Lett.* **11** 2510–6
[24] Yasbolaghi R and Khoei A 2020 *Eng. Fract. Mech.* **226** 106848
[25] Pugno N, Ciavarella M, Cornetti P and Carpinteri A 2006 *J. Mech. Phys. Solids* **54** 1333–49
[26] Paris P C 1961 *Trends Eng.* **13** 9–14
[27] Paris P and Erdogan F 1963 *J. Basic Eng.* **85** 528–33
[28] Somà A and De Pasquale G 2009 *J. Microelectromech. Syst.* **18** 828–35
[29] Somà A and De Pasquale G 2010 Reliability of MEMS: effects of different stress conditions and mechanical fatigue failure detection *2010 Proc. 6th Int. Conf. on Perspective Technologies and Methods in MEMS Design (Lviv, Ukraine, 2010)* (IEEE) pp 72–80
[30] De Pasquale G, Somà A and Ballestra A 2008 Mechanical fatigue on gold MEMS devices: experimental results *2008 Symp. on Design, Test, Integration and Packaging of MEMS/MOEMS (Nice, France, 2008)* (IEEE) pp 11–15
[31] De Pasquale G, Somà A and Ballestra A 2009 *Analog Integr. Circuits Signal Process.* **61** 215–22
[32] De Pasquale G and Somà A 2013 *Frat. Integrita Strutt.* **7** 114–26
[33] De Pasquale G and Somà A 2011 *J. Microelectromech. Syst.* **20** 1054–63
[34] Kahn H, Ballarini R, Bellante J and Heuer A 2002 *Science* **298** 1215–8
[35] Alter A L, Flader I B, Chen Y, Ortiz L C, Shin D D and Kenny T W 2020 *J. Microelectromech. Syst.* **29** 1483–92
[36] Chang C-C and Chiang K-N 2020 *J. Electron. Packag.* **142** 011005
[37] Takashima K, Halford T P and Higo Y 2005 Fracture and fatigue testing of micro-sized materials for MEMS applications *Proc. ASME 2005 Pacific Rim Technical Conf. and Exhibition on Integration and Packaging of MEMS, NEMS, and Electronic Systems Collocated with the ASME 2005 Heat Transfer Summer Conf. Advances in Electronic Packaging, Parts A, B, and C (San Francisco, California, 17–22 July 2005)* pp 1679–83
[38] Son D, Kim J-J, Kim J-Y and Kwon D 2005 *Mater. Sci. Eng.* A **406** 274–8
[39] Le Huy V, Kamiya S, Gaspar J and Paul O 2019 *Microsyst. Technol.* **25** 2713–26
[40] Connally J and Brown S 1991 Micromechanical fatigue testing *TRANSDUCERS '91: 1991 Int. Conf. on Solid-State Sensors and Actuators. Digest of Technical Papers (San Francisco, CA, USA, 1991)* pp 953–6
[41] Wu J-Y and Chen W-X 2021 *Comput. Methods Appl. Mech. Eng.* **387** 114125
[42] Corigliano A, Ghisi A, Langfelder G, Longoni A, Zaraga F and Merassi A 2011 *Eur. J. Mech.* A **30** 127–36
[43] Auersperg J, Auerswald E, Collet C, Dean T, Vogel D, Winkler T and Rzepka S 2018 *Microelectron. Reliab.* **87** 238–44
[44] Bergan P and Aamodt B 1974 *Nucl. Eng. Des.* **29** 180–8

[45] Somà A, De Pasquale G, Brusa E and Ballestra A 2010 *Strain* **46** 358–73
[46] Somà A and Saleem M 2018 *J. Micromech. Microeng.* **29** 025004
[47] Somà A, Pistorio F and Saleem M M 2022 *J. Micromech. Microeng.* **32** 025006
[48] Margesin B, Bagolini A, Guarnieri V, Giacomozzi F, Faes A, Pal R and Decarli M 2003 Stress characterization of electroplated gold layers for low temperature surface micromachining *Symp. on Design, Test, Integration and Packaging of MEMS/MOEMS 2003* (*Cannes, France, 2003)* (IEEE) pp 402–5
[49] Kal S, Bagolini A, Margesin B and Zen M 2006 *Microelectron. J.* **37** 1329–34
[50] Somà A and Saleem M M 2015 *J. Micromech. Microeng.* **25** 055007
[51] Saleem M M and Somà A 2015 *Microelectron. Reliab.* **55** 2284–98
[52] Somà A, Saleem M, Margesin B and Armando M 2019 *Microsyst. Technol.* **25** 2525–33
[53] Zhang W M, Yan H, Peng Z K and Meng G 2014 *Sens. Actuators* A **214** 187–218
[54] Tada H, Paris P C and Irwin G R 2000 *The Stress Analysis of Cracks Handbook* 3rd edn (ASME Press) (https://doi.org/10.1115/1.801535)
[55] Richard H A, Buchholz F G, Kullmer G and Schöllmann M 2003 2d-and 3d-mixed mode fracture criteria *Key Eng. Mater.* **251** 251–60
[56] Anderson T L 2017 *Fracture Mechanics: Fundamentals And Applications* (Boca Raton, FL: CRC Press)
[57] Rice J R 1968 *J. Appl. Mech.* **35** 379–86
[58] Yau J, Wang S and Corten H 1980 *J. Appl. Mech.* **47** 335–41
[59] Yu H and Kuna M 2021 *Eng. Fract. Mech.* **249** 107722
[60] Tanaka K 1974 *Eng. Fract. Mech.* **6** 493–507
[61] Irwin G R 1957 *J. Appl. Mech.* **24** 361–4
[62] Xiangqiao Y, Shanyi D and Zehua Z 1992 *Eng. Fract. Mech.* **43** 471–5
[63] DEMIR O, Ayhan A O, IRIC S and Lekesiz H 2018 *Chin. J. Aeronaut.* **31** 1525–34
[64] Hussain M, Pu S and Underwood J 1974 *Fracture Analysis: Proc. of the 1973 National Symp. on Fracture Mechanics, Part II 1973* (https://doi.org/10.1520/STP560-EB)
[65] Erdogan F and Sih G 1963 *J. Basic Eng.* **85** 519–25
[66] Wu C H 1978 *J. Appl. Mech.* **45** 553–8
[67] Sih G C 1974 *Int. J. Fract.* **10** 305–21
[68] Richard H, Schramm B and Schirmeisen N-H 2014 *Int. J. Fatigue* **62** 93–103
[69] Somà A and Ballestra A 2009 *J. Micromech. Microeng.* **19** 095023
[70] Barsoum R S 1976 *Int. J. Numer. Methods Eng.* **10** 25–37
[71] Speidel M O 1979 *Gold Bul.* **12** 145–8
[72] Lee S, Kim Y Y and Cho Y 2017 *Coatings* **7** 143
[73] Zhao Y, Zheng J, Liu J, Holmes J W, Liu L and Sha J 2018 *Mater. Sci. Eng.* A **716** 28–36
[74] Hertzberg R W, Vinci R P and Hertzberg J L 2020 *Deformation and Fracture Mechanics of Engineering Materials* (New York: Wiley))
[75] Schneider D and Tucker M 1996 *Thin Solid Films* **290** 305–11
[76] Lee C-W, Liu L and Holmes J 2013 *Fatigue Fract. Eng. Mater. Struct.* **36** 1187–98
[77] Jensen B D, de Boer M P, Masters N D, Bitsie F and LaVan D A 2001 *J. Microelectromech. Syst.* **10** 336–46
[78] Tariq Jan M, Hisham Bin Hamid N, Md Khir M H, Ashraf K and Shoaib M 2014 *J. Qual. Reliab. Eng.* **2014** 1–16
[79] Shackelford J F and Alexander W 2000 *CRC Materials Science and Engineering Handbook* (Boca Raton, FL: CRC Press)
[80] Sommer N, Stredak F, Wiegand M and Böhm S 2022 *Weld. World* **67** 1–12
[81] De Pasquale G and Somà A 2010 *Mech. Syst. Signal Process.* **24** 1621–33